DOI: 10.1002/adma.200601215

Self-Assembled Growth of $BiFeO_3$–$CoFe_2O_4$ Nanostructures**

By *Haimei Zheng*,* *Florian Straub*, *Qian Zhan*, *Pei-Ling Yang*, *Wen-Kuo Hsieh*, *Florin Zavaliche*, *Ying-Hao Chu*, *Uli Dahmen*, and *Ramamoorthy Ramesh*

Multifunctional materials have attracted increasing interest in recent years because of their potential applications in novel technological devices.[1–11] Typically, they have more than one of the order parameters that can couple to each other. $BiFeO_3$–$CoFe_2O_4$ is such a model multifunctional system, with ferroelectricity (from $BiFeO_3$) and ferrimagnetism (from $CoFe_2O_4$) that couple to each other through a stress mediation. We have recently demonstrated that $BiFeO_3$–$CoFe_2O_4$ self-assembles into nanostructures with $CoFe_2O_4$ nanopillars heteroepitaxially embedded in a $BiFeO_3$ matrix on (001) $SrTiO_3$ substrates. Such nanostructures show significant magnetoelectric coupling.[12] The ferroelectric and magnetic properties as well as the degree of the coupling are critically dependent on the morphology of the nanostructures, including domain patterns and shapes as well as the interfaces. In order to pursue the enhanced multifunctionality, significant effort has been made on understanding the growth mechanism and controlling the morphology of the nanostructures.

The morphology adopted by a crystalline material when it nucleates on a substrate surface is one of the fundamental issues of heteroepitaxy. Depending on the surface energy terms, i.e., substrate surface energy γ_1, interface energy γ_{12}, and surface energy of the crystalline phase γ_2, the equilibrium shape of a crystalline nucleus on a substrate can be determined using the Winterbottom construction.[13] The possible configuration of the crystalline nucleus on the substrate is a Wulff shape that has been cut off by the substrate, translated by the signed distance $\Delta\gamma$ from the origin. $\Delta\gamma$ is the wetting strength, which is the energy difference obtained by replacing the substrate surface with an interface, $\Delta\gamma = \gamma_{12} - \gamma_1$. In the $BiFeO_3$–$CoFe_2O_4$ system, $BiFeO_3$ has a distorted perovskite structure ($R3c$)[14] and $CoFe_2O_4$ has a cubic spinel structure ($Fd3m$). $CoFe_2O_4$ is characterized by the lowest surface energy of {111} surfaces, which is reflected in an equilibrium shape of an octahedron bounded by eight {111} facets.[15,16] In contrast, most perovskite phases have the lowest energy surfaces of {001} surfaces and a corresponding equilibrium shape of a cube dominated by six {100} facets.[17–20] Because of the difference in the surface energy anisotropy in $BiFeO_3$ and $CoFe_2O_4$ the two phases can display different growth modes on a substrate surface. We estimate the morphology of the $BiFeO_3$–$CoFe_2O_4$ nanostructures grown on a substrate surface using the Winterbottom construction. Figure 1 is the Winterbottom construction of the $BiFeO_3$ and $CoFe_2O_4$ phases nucleating on single-crystal substrates as a function of the substrate orientation. For simplification, we assumed a wetting strength of $\Delta\gamma = \gamma_2$ for both phases. On a (001) oriented substrate, $BiFeO_3$ wets the substrate completely and follows a layer-by-layer growth; in contrast, $CoFe_2O_4$ partially wets the substrate and forms islands bonded by four {111} surfaces. In the subsequent growth, each phase grows on top of its own phase, which leads to $CoFe_2O_4$ pillars embedded in a $BiFeO_3$ matrix. On a (111) oriented substrate, $CoFe_2O_4$ displays layer-by-layer growth and $BiFeO_3$ forms islands characterized with three {100} surfaces. At a later growth stage, $BiFeO_3$ grows into pillars embedded in a $CoFe_2O_4$ matrix. When the substrate orientation

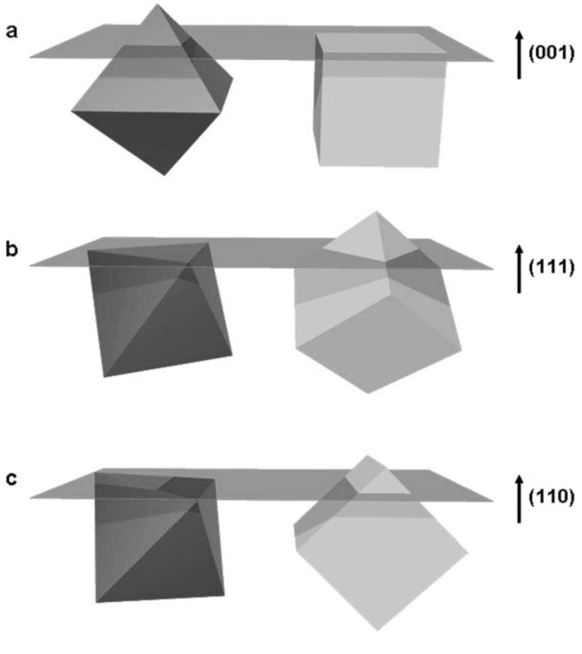

Figure 1. Winterbottom construction of $CoFe_2O_4$ (left) and $BiFeO_3$ (right) nucleating on a) (001), b) (111), and c) (110) $SrTiO_3$ surfaces.

---

[*] Dr. H. Zheng, F. Straub, Dr. Q. Zhan, P.-L. Yang, Dr. F. Zavaliche, Dr. Y.-H. Chu, Prof. R. Ramesh
Department of Materials Science and Engineering and
Department of Physics, University of California
Berkeley, CA 94720 (USA)
E-mail: haimei@berkeley.edu
Dr. W.-K. Hsieh, Dr. U. Dahmen
National Center for Electron Microscopy
Lawrence Berkeley National Laboratory
Berkeley, CA 94720 (USA)

[**] This work is supported by ONR MURI under contract No. E-21-6RU-G4 and LBNL-LDRD. The authors acknowledge the support of the National Center for Electron Microscopy, Lawrence Berkeley Lab, which is supported by the U.S. Department of Energy under Contract # DE-AC02–05CH11231.

is not parallel to the lowest energy surface of either phase, both $BiFeO_3$ and $CoFe_2O_4$ phases could have comparable wetting configuration with similar nucleation barriers. In this case, both phases have island growth modes, for example, on a (110) oriented substrate. As a consequence of the competing wetting conditions, the film can form a maze pattern in which neither phase can be identified as the matrix or pillars.

Based on the above estimation, we have explored the growth of the $BiFeO_3$–$CoFe_2O_4$ nanostructures on $SrTiO_3$ substrates with (001), (111), or (110) orientations. On each substrate, we have studied the effects of changing the volume fraction of the two phases (65:35, 1:1, and 33:67 of $BiFeO_3$/$CoFe_2O_4$) on the nanostructures. Because the morphologies of the $BiFeO_3$–$CoFe_2O_4$ nanostructures are critically dependent on the growth conditions, the growth kinetics of the nanostructures have also been studied. The magnetic and ferroelectric properties as well as the coupling of the $BiFeO_3$–$CoFe_2O_4$ nanostructures that depends on the morphologies of the nanostructures will be reported separately. Because similar nanostructures that are formed by self-assembly have been observed in many other systems,[21,22] we believe that this report on the growth of the $BiFeO_3$–$CoFe_2O_4$ nanostructures is very valuable to our knowledge on the growth and the control of nanostructural materials.

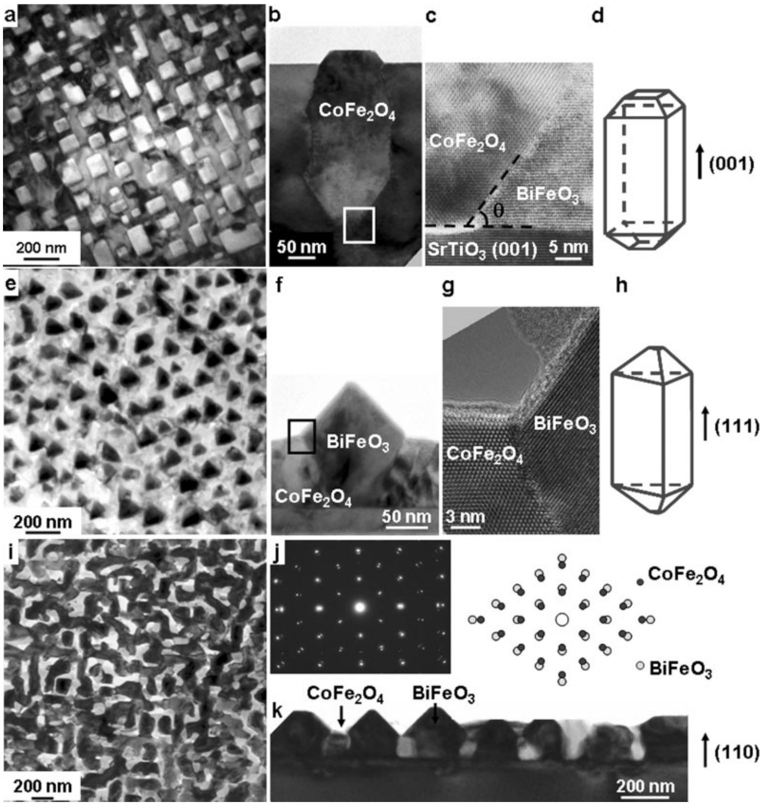

Figure 2. Morphologies of the $BiFeO_3$–$CoFe_2O_4$ nanostructures (volume fraction of 1:1) grown on a–d) a (001) $SrTiO_3$ substrate at 700 °C, e–h) a (111) $SrTiO_3$ substrate at 650 °C, and i–k) a (110) $SrTiO_3$ substrate at 700 °C. a) A plan-view bright-field transmission electron microscopy (TEM) image showing rectangular-shaped $CoFe_2O_4$ (bright) in a $BiFeO_3$ (dark) matrix. b) A cross-sectional TEM image of a single $CoFe_2O_4$ pillar embedded in a $BiFeO_3$ matrix. c) A high-resolution TEM image from the interface region marked by the rectangle in (b). d) A schematic of a $CoFe_2O_4$ nanopillar. e) A plan-view bright-field TEM image showing triangular-shaped $BiFeO_3$ (dark) in a $CoFe_2O_4$ (bright) matrix. f) A cross-sectional TEM image of a single $BiFeO_3$ pillar embedded in a $CoFe_2O_4$ matrix. g) A high-resolution TEM image from the interface region marked by the rectangle in (f). h) A schematic of a $BiFeO_3$ pillar. i) A plan-view bright-field TEM image showing a maze pattern of $BiFeO_3$ (dark) and $CoFe_2O_4$ (bright). j) Selected area diffraction pattern from (i) and a schematic showing the epitaxy of $BiFeO_3$ and $CoFe_2O_4$ phases. k) The corresponding cross-sectional TEM image.

The morphologies of the $BiFeO_3$–$CoFe_2O_4$ nanostructures (volume fraction of 1:1) grown on (001)-, (111)-, and (011)-oriented $SrTiO_3$ substrates are shown in Figure 2. On the (001) $SrTiO_3$ substrate, $CoFe_2O_4$ forms nanopillars embedded in a $BiFeO_3$ matrix (Fig. 2a–d). Rectangular shaped $CoFe_2O_4$ nanopillars and {110}-type interfaces with the matrix are observed (Fig. 2a). $CoFe_2O_4$ nanopillars change their shape across the film thickness, which is shown in the cross-sectional transmission electron microscopy (TEM) images and the schematic of a pillar (Fig. 2b–d). Within a 100 nm film thickness, the width of the $CoFe_2O_4$ pillar increases, resulting in an inverted cone shape at the substrate interface. The rest of the pillar maintains roughly the same lateral dimensions within the $BiFeO_3$ matrix. There are sharp interfaces between the two phases as well as between the substrate and the two phases. No obvious interdiffusion was observed across the interface from energy-dispersive spectroscopy (EDS) studies. On the top of the film, the $CoFe_2O_4$ pillar forms an island with characteristic facets. The facet planes are 54.7° with respect to the (001) plane indicating {111}-type facets.

The structure of the matrix phase and the pillar phase is inverted in the nanostructures grown on a (111) $SrTiO_3$ substrate. $BiFeO_3$ forms triangular shaped nanopillars embedded in a $CoFe_2O_4$ matrix (Fig. 2e–h). All the $BiFeO_3$ nanopillars have the same crystallographic orientation and have {112} interfaces with the $CoFe_2O_4$ matrix. Similar inverted cone shaped $BiFeO_3$ pillars at the substrate interface were observed. Figure 2f is a cross-sectional TEM image of a single $BiFeO_3$ pillar from a 100 nm thick film. The lateral dimensions of the $BiFeO_3$ pillar continuously increase from the substrate interface and reaches a constant value at a certain film thickness. A high-resolution TEM image of the interface between a $BiFeO_3$ pillar and matrix shows the change of the slope (Fig. 2g). $BiFeO_3$ pillars form islands with {100} facets on the top of the film.

As it was predicted from the above Winterbottom construction, a maze pattern with entangled $BiFeO_3$ and $CoFe_2O_4$ phases was observed on a (011)-oriented $SrTiO_3$ substrate (Fig. 2i–k). Figure 2i is a plan-view TEM image showing the morphology of the nanostructures. The corresponding electron diffraction pattern shows only $BiFeO_3$ and $CoFe_2O_4$ phases that are epitaxial to the substrate (Fig. 2j). A cross-sectional TEM image shows that both phases grew from the substrate surface to the top of the film (Fig. 2g). Unlike the nanostructures grown on (001) and (111) substrates, the two phases on the (110) substrate keep a relatively constant volume fraction across the film thickness. The "columnar" shape of both phases in the cross section suggest that a similar morphological pattern is maintained in the film close to the substrate interface and on the top of the film.

The distinct different morphologies of the $BiFeO_3$–$CoFe_2O_4$ nanostructures on (001)-, (110)-, and (111)-oriented substrates are consistent with the Winterbottom construction in Figure 1. The large difference in the surface energy anisotropy of the $BiFeO_3$ and $CoFe_2O_4$ phases results in the different nucleation modes of the two phases on a substrate. On both the (100) and (111) oriented substrates, the wetting phase covers a large area of the substrate and the partially wetting phase forms islands at the initial nucleation stage. We have observed the early stage morphologies of the nanostructures (ca. 5 nm film thickness) that show the relatively small dimensions of the islands. The subsequent growth establishes the area fraction of the two phases close to the volume fraction of the two phases. We believe that the facets of the pillars close to the substrate interface prefer the lowest energy interfaces of the two phases. We have also observed that the facet is the (111) surface of the $CoFe_2O_4$ phase in Figure 2c. However, different facets have also been observed in other pillars. A detailed study on the facets of inverted cone shaped pillars at the substrate interface is needed in future work. For the nanostructures grown on (110) substrates, because the two phases have similar wetting conditions (and similar island growth modes), the area fraction of the two phases is established at an early stage and there is no distinct change in their area fraction within the film thickness.

The atomic force microscopy (AFM) phase-contrast images and their schematics show the topographic facets of $BiFeO_3$–$CoFe_2O_4$ nanostructures with a 1:1 volume fraction grown on (001)-, (111)-, and (110)-oriented $SrTiO_3$ substrates (Fig. 3). The facets and interfaces of islands have been identified based on both AFM and TEM studies. On the (001) oriented substrate, $CoFe_2O_4$ forms islands and $BiFeO_3$ is flat at the film surface. $CoFe_2O_4$ islands have (001) end facets and (111), $(1\bar{1}1)$, $(\bar{1}\bar{1}1)$ and $(\bar{1}11)$ side facets. The interfaces with the $BiFeO_3$ matrix are {110} planes. The aspect ratio of the islands, h/a (defined in Figure 3a), is dependent on the growth temperature (T) and growth rate (v). On the (111) substrate, $BiFeO_3$ forms islands and $CoFe_2O_4$ has a flat surface. $BiFeO_3$ islands have a (111) end facet (with a negligible area fraction) and (001), (010), and (100) side facets. The interfaces with the $CoFe_2O_4$ matrix are {112} planes. On the (110)-oriented substrate, both $BiFeO_3$ and $CoFe_2O_4$ phases form facets. $BiFeO_3$ mostly forms hut-shaped islands with the (110) end facet and the (001), (010), $(00\bar{1})$, and (100) side facets. We believe the facets of the $CoFe_2O_4$ phase are {111}-type, however, they are not clearly identified from Figure 3c. $BiFeO_3$ has a higher geometry than $CoFe_2O_4$, which is probably because of the slight difference in their wetting properties on the (110) substrate. The observed topographic shape and facets of the $BiFeO_3$–$CoFe_2O_4$ nanostructures agree very well with the Winterbottom construction based on the surface energy isotropy.

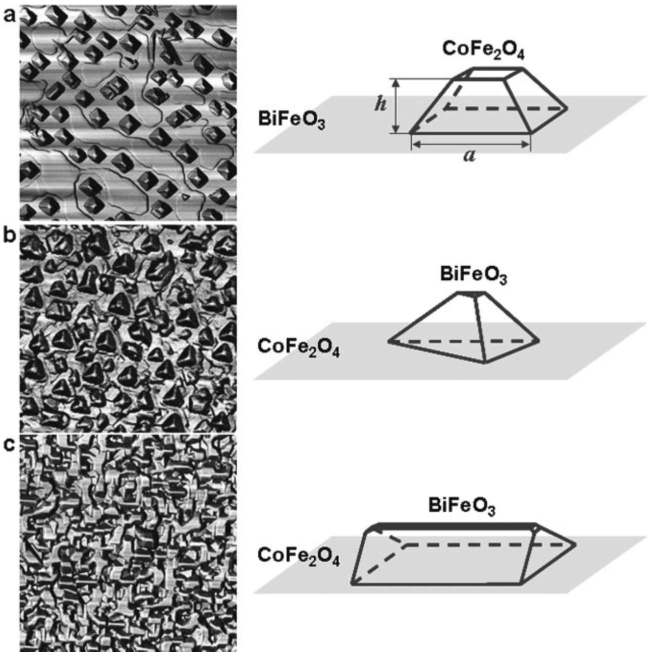

Figure 3. AFM phase-contrast images of $BiFeO_3$–$CoFe_2O_4$ nanostructures (volume fraction of 1:1) grown on a) (001), b) (111), and c) (110) oriented $SrTiO_3$ substrates. All images are 2.5 μm × 2.5 μm. The schematics show the shape and facets of the islands. On the (001) substrate, $CoFe_2O_4$ has a (001) end facet and (111), $(1\bar{1}1)$, $(\bar{1}11)$, and $(\bar{1}\bar{1}1)$ side facets. On the (111) substrate, $BiFeO_3$ has a (111) end facet and (001), (010), and (100) side facets. On the (110) substrate, $BiFeO_3$ has a (110) top end facet and (001), (010), $(00\bar{1})$, and (100) side facets.

It is further found that the volume fraction of the two phases did not introduce distinct changes in the morphologies of the $BiFeO_3$–$CoFe_2O_4$ nanostructures. For example, irrespective of the volume fraction, $CoFe_2O_4$ forms nanopillars in a $BiFeO_3$ matrix on a (001)-oriented substrate, $BiFeO_3$ forms nanopillars in a $CoFe_2O_4$ matrix on a (111)-oriented substrate, and $BiFeO_3$ and $CoFe_2O_4$ form a maze pattern on a (110)-oriented substrate (Fig. 4). It is clear that differences in anisotropic strain,[8] surface stress, and surface diffusivity[23] can result in differences in the morphologies of the nanostructures with different compositions. In addition, the size and spacing of nanostructures are restricted to their growth kinetics (e.g., growth rate, temperature), which will be discussed below. Therefore, some differences in the details of the morphologies are observed in the nanostructures with different volume fractions (Fig. 4a–c, d–f, and g–i). The fact that the volume fraction of the two phases does not change their growth modes validates our growth model based on surface energy anisotropy using the Winterbottom construction.

At growth temperatures in the range of 550–700 °C and growth rates of 0.5–8 $nm\,min^{-1}$, the dimensions of the

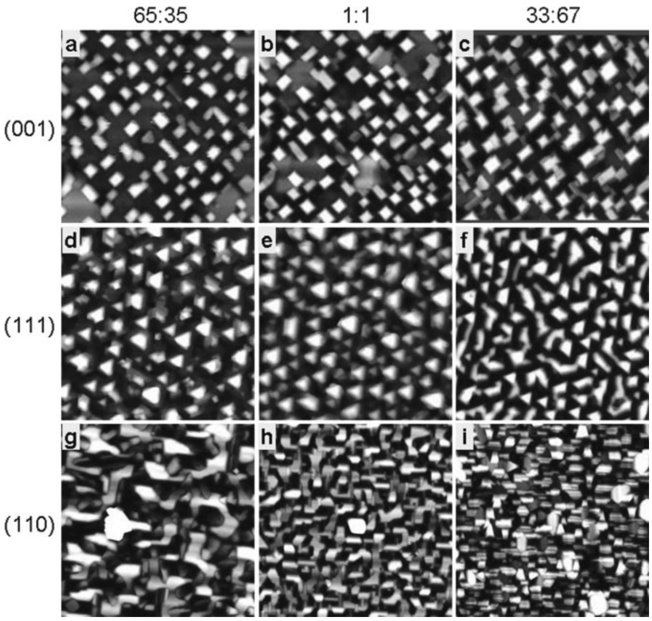

Figure 4. AFM images of $BiFeO_3$–$CoFe_2O_4$ nanostructures with volume fractions of 65:35, 1:1, and 33:67 grown on a–c) (001) substrates at 700 °C; d–f) (111) substrates at 650 °C, and g–i) (110) substrates at 700 °C. All images are 3 µm × 3 µm.

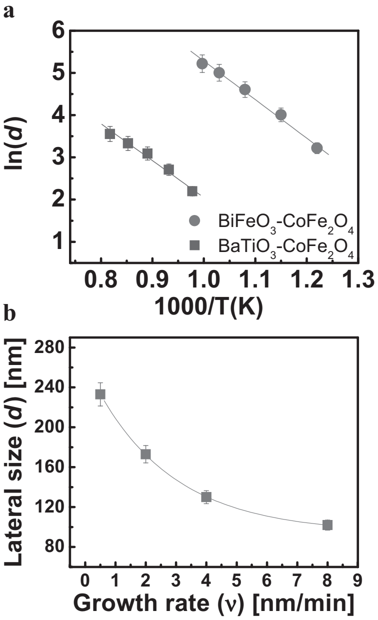

Figure 5. a) Temperature dependence of $BiFeO_3$–$CoFe_2O_4$ and $BaTiO_3$–$CoFe_2O_4$ [24] nanostructures grown on (001)-oriented $SrTiO_3$ substrates. *d* is the lateral dimension of the $CoFe_2O_4$ nanopillars. The line is a linear fit. b) Growth rate dependence of $BiFeO_3$–$CoFe_2O_4$ nanostructures grown on (001) oriented $SrTiO_3$ substrates. The line is a second-order fit.

$BiFeO_3$–$CoFe_2O_4$ nanostructural features increase as the growth temperature increases and decrease as the growth rate increases. A lower growth temperature and/or a higher growth rate induces supersaturated perovskite type phases (metastable). We found that these trends are applicable to all $BiFeO_3$–$CoFe_2O_4$ nanostructures with different volume fractions on differently oriented substrates (with slight difference in temperature and growth rate ranges). We focus on the kinetics of $BiFeO_3$–$CoFe_2O_4$ nanostructures with a volume fraction of 1:1 grown on (001) substrates. At a constant growth rate of 4 nm min^{-1}, the lateral size of the $CoFe_2O_4$ pillars versus the growth temperatures is plotted in Figure 5a. The lateral size of the pillars (ln(*d*)) decreases as the growth temperature decreases, which can be fitted into a linear plot, $\ln(d) \propto 1/T$. For comparison, we also plotted the temperature dependence of $CoFe_2O_4$ nanopillar size from a $BaTiO_3$–$CoFe_2O_4$ system from an earlier publication.[24] It is interesting that a similar trend and fitting has been observed in both cases. Figure 5b plots the lateral size of the $CoFe_2O_4$ pillars versus the growth rates at a constant growth temperature of 700 °C. The lateral size of the pillars (*d*) decreases as the growth rate increases, which can be fitted into a second order plot, $d^2 \propto 1/v$.

The growth of the $BiFeO_3$–$CoFe_2O_4$ nanostructures can be modeled as a diffusion process. In a steady-state growth of the nanostructures, the multicomponent species come to the film surface and phase-separate into nanostructures. The nanostructures are formed at the film surface and subsequently incorporated into the bulk film. Transport is limited to the advancing solid–vapor interface, and diffusion within the bulk film is negligible. This has been confirmed by the result that no obvious changes were observed after the nanostructures were annealed at the film growth temperatures for 10 h. For the 2D diffusion, we simply use the standard equation

$$<x^2 + y^2> = 4\tilde{D}t \tag{1}$$

where $<x^2 + y^2>^{1/2}$ is the mean diffusion distance, $\tilde{D}$ is the diffusion coefficient

$$\tilde{D} = \tilde{D}_0 e^{-\frac{E_a}{kT}} \tag{2}$$

E_a is the activation energy, k is the Boltzmann constant, T is the temperature, t is the time, $t = 1/v$, and v is the growth rate. If we assume that the size of the pillars is approximately equal to the diffusion distance, $d \sim <x^2 + y^2>^{1/2}$, Equation 1 can be expressed as

$$d^2 = 4\tilde{D}_0 e^{-\frac{E_a}{kT}} \frac{1}{v} \tag{3}$$

Therefore, at a constant growth rate, the size of the pillars (ln(*d*)) is proportional to $1/T$, which can be expressed by

$$\ln d = A - B\frac{1}{T} \tag{4}$$

where A and B are constants, $B = E_a/2kT$.

At a constant growth temperature, the size of pillars (d^2) is inversely proportional to the growth rate, which can be expressed as

$$d^2 = C\frac{1}{v} \tag{5}$$

where C is constant,

$$C = 4\tilde{D}_0 e^{-\frac{E_a}{kT}} \tag{6}$$

This analysis based on diffusion agrees well with our experimental observations in Figure 5. The temperature dependence of the $CoFe_2O_4$ nanopillars for the $BiFeO_3$–$CoFe_2O_4$ system gives an activation energy of 0.83 eV, yielding an activation energy for diffusion of 1.66 eV. Such an activation energy for diffusion is close to the value (1.56 eV) calculated for the $BaTiO_3$–$CoFe_2O_4$ nanostructures. We further calculated the activation energy from the temperature dependence of the size of the $BiFeO_3$ nanopillars (also a linear plot) in the $BiFeO_3$–$CoFe_2O_4$ nanostructures grown on (111) substrates. A smaller activation energy value (0.58 eV) for diffusion was obtained. We believe that the calculated activation energy corresponds to the diffusion barrier for the formation of nanopillars. For example, the relatively high volatility of Bi may induce a lower activation energy of the $BiFeO_3$ nanopillars. We also believe that step growth is unlikely to be the limiting factor for the growth of $BiFeO_3$–$CoFe_2O_4$ nanostructures. This is based on the fact that the activation energy for $CoFe_2O_4$ nanopillars are similar for both $BiFeO_3$–$CoFe_2O_4$ and $BaTiO_3$–$CoFe_2O_4$ nanostructures but the facets of the $CoFe_2O_4$ nanopillars are very different ($CoFe_2O_4$ islands are in a dome shape in $BaTiO_3$–$CoFe_2O_4$ nanostructures[24] and they have distinct {111} facets in $BiFeO_3$–$CoFe_2O_4$ nanostructures). A similar diffusion mechanism was used to understand the phase separation in Al–Ge films by Atzmon and co-workers,[25,26] from which the calculated activation energy is consistent with the surface diffusion barrier of Al and Ge. We are aware that in our case the activation energies for $CoFe_2O_4$ are relatively high (above 1 eV) and only a slight difference was observed in the values for $BaTiO_3$–$CoFe_2O_4$ and $BiFeO_3$–$CoFe_2O_4$ nanostructures, although there is about 200 °C difference in the growth temperature. For the growth of nanostructures with different structures and multiple components, the surface steps, exchange mechanisms,[27] and other factors may have to be considered as diffusion barriers.

In summary, we have investigated the $BiFeO_3$–$CoFe_2O_4$ nanostructures with volume fractions of 65:35, 1:1, and 33:67 grown on $SrTiO_3$ substrates with (100), (111), and (110) orientations. Unique morphologies, obtained irrespective of the volume fraction, have been observed on each substrate. The dependence of the morphologies of the $BiFeO_3$–$CoFe_2O_4$ nanostructures on the substrate orientations is attributed to the different growth modes of the two phases. We also studied the growth kinetics of the $BiFeO_3$–$CoFe_2O_4$ nanostructures. A higher growth temperature and/or a slower growth rate induces larger-sized nanopillars. The $BiFeO_3$–$CoFe_2O_4$ is a model system for the growth and control of two-phase nanostructures. The $BiFeO_3$–$CoFe_2O_4$ nanostructures are ideal for the future study on the morphological dependence of magnetoelectric coupling.

Experimental

$BiFeO_3$–$CoFe_2O_4$ nanostructures were grown using pulsed laser deposition (PLD) with a KrF ($\lambda = 248$ nm) excimer laser with a laser density of 1.2 $J\,cm^{-2}$. A dynamic chamber pressure of 100 mTorr (1 Torr ≈ 133.3 Pa) O_2 was maintained during deposition. A single Bi–Co–Fe–Oxide ceramic target was used. After the deposition, samples were cooled to room temperature in 1 atm (1 atm = 101 325 Pa) oxygen at a cooling rate of 5 °C min^{-1}. For each of the (001), (111), and (110) substrates, we studied $BiFeO_3$–$CoFe_2O_4$ nanostructures with $BiFeO_3/CoFe_2O_4$ volume fraction of 65:35, 1:1, and 33:67. The substrate temperatures were in the range of 450–750 °C, growth rate of 0.5–16 nm min^{-1}, and film thickness of 5–200 nm. Nanostructures were characterized using X-ray diffraction (XRD), atomic force microscopy (AFM), and transmission electron microscopy (TEM). The transmission electron microscopes used were a JOEL 3010 operating at 300 kV, Philips CM300, and Philips CM200 equipped with an EDS detector.

Received: June 5, 2006
Final version: July 26, 2006

---

[1] P. Murugavel, P. Padhan, W. Prellier, *Appl. Phys. Lett.* **2004**, *85*, 4992.
[2] T. Lottermoser, T. Lonkai, U. Amann, D. Hohlwein, J. Ihringer, M. Fiebig, *Nature* **2004**, *430*, 541.
[3] H. Zheng, J. Wang, S. E. Lofland, Z. Ma, L. Mohaddes-Ardabili, T. Zhao, L. Salamanca-Riba, S. R. Shinde, S. B. Ogale, F. Bai, D. Viehland, Y. Jia, D. G. Schlom, M. Wuttig, A. Roytburd, R. Ramesh, *Science* **2004**, *303*, 661.
[4] N. A. Spaldin, M. Fiebig, *Science* **2005**, *309*, 391.
[5] M. P. Singh, W. Prellier, C. Simon, B. Raveau, *Appl. Phys. Lett.* **2005**, *87*, 022 505.
[6] S. X. Dong, J. Y. Zhai, N. G. Wang, F. M. Bai, J. F. Li, D. Vieland, T. A. Lograsso, *Appl. Phys. Lett.* **2005**, *87*, 222 504.
[7] N. G. Wang, J. Cheng, A. Pyatakov, A. K. Zvezdin, J. F. Li, L. E. Cross, D. Vieland, *Phys. Rev. B: Condens. Matter Mater. Phys.* **2005**, *72*, 104 434.
[8] C. W. Nan, G. Liu, Y. H. Lin, H. D. Chen, *Phys. Rev. Lett.* **2005**, *94*, 197 203.
[9] J. Slutsker, I. Levin, J. H. Li, A. Artemev, A. L. Royburd, *Phys. Rev. B: Condens. Matter Mater. Phys.* **2006**, *73*, 184 127.
[10] T. Wu, M. A. Zurbuchen, S. Saha, R. V. Wang, S. K. Streiffer, J. F. Mitchell, *Phys. Rev. B: Condens. Matter Mater. Phys.* **2006**, *73*, 134 416.
[11] Y. Yamasaki, S. Miyasaka, Y. Kaneko, J. P. He, T. Arima, Y. Tokura, *Phys. Rev. Lett.* **2006**, *96*, 249 902.
[12] F. Zavaliche, H. Zheng, L. Mohaddes-Ardabili, S. Y. Yang, Q. Zhan, P. Shafer, E. Reilly, R. Chopdekar, Y. Jia, P. Wright, D. G. Schlom, Y. Suzuki, R. Ramesh, *Nano Lett.* **2005**, *5*, 1793.
[13] W. L. Winterbottom, *Acta Metall.* **1967**, *15*, 303.
[14] C. Michel, J. M. Moreau, G. D. Achenbac, R. Gerson, W. J. James, *Solid State Commun.* **1969**, *7*, 701.
[15] R. K. Mishra, G. J. Thomas, *J. Appl. Phys.* **1977**, *48*, 4576.
[16] G. Wulff, *Z. Kristallogr. Mineral.* **1901**, *34*, 449.
[17] J. Padilla, D. Vanderbilt, *Phys. Rev. B: Condens. Matter Mater. Phys.* **1997**, *56*, 1625.
[18] B. Meyer, J. Padilla, D. Vanderbilt, *Faraday Discuss.* **1999**, *114*, 395.
[19] T. Sano, D. M. Saylor, G. S. Rohrer, *J. Am. Ceram. Soc.* **2003**, *86*, 1933.
[20] M. Alfredsson, J. P. Brodholt, D. P. Dobson, A. R. Oganov, C. R. A. Catlow, S. C. Parker, G. D. Price, *Phys. Chem. Miner.* **2005**, *31*, 671.
[21] M. Grundmann, J. Christen, N. N. Ledentsov, J. Bohrer, D. Bimberg, S. S. Ruvimov, P. Werner, U. Richter, U. Gosele, J. Heydenreich, V. M. Ustinov, A. Y. Egorov, A. E. Zhukov, P. S. Kopev, Z. I. Alferov, *Phys. Rev. Lett.* **1995**, *74*, 4043.

[22] V. Moshnyaga, B, Damaschke, O. Shapoval, A. Belenchuk, J. Faupel, O. I. Lebedev, J. Verbeeck, G. Van Tendeloo, M. Mucksch, V. Tsurkan, R. Tidecks, K. Samwer, *Nat. Mater.* **2003**, *2*, 247.

[23] S. P. A. Gill, *Thin Solid Films* **2003**, *423*, 136.

[24] H. Zheng, J. Wang, L. Mohaddes-Ardabili, D. G. Schlom, M. Wuttig, L. Salamanca-Riba, R. Ramesh, *Appl. Phys. Lett.* **2004**, *85*, 2035.

[25] C. D. Adams, M. Atzmon, Y.-T. Cheng, D. J. Srolovitz, *J. Mater. Res.* **1992**, *7*, 653.

[26] M. Atzmon, D. A. Kessler, D. J. Srolovitz, *J. Appl. Phys.* **1992**, *72*, 442.

[27] D. J. Harris, M. Y. Lavrentiev, J. H. Harding, N. L. Allan, J. A. Purton, *J. Phys.: Condens. Matter* **2004**, *16*, L187.